PERFORMANCE OF A CONICAL TWO-SOLENOID FOCUSING SYSTEM FOR LASER-DRIVEN PROTONS

Laura-Anamaria Nălbaru[1*], Michaela Arnold[2], Cătălin M. Ticoş[3]

Charged particle beam acceleration techniques are rapidly evolving alongside advances in high-power laser technology. Laser-driven acceleration of charged particles is emerging as a compact alternative to conventional and costly radio-frequency accelerators, enabling particle generation through simple target configurations. However, the beams produced by these systems possess unique characteristics that create both opportunities and challenges for practical implementation. One field where laser-plasma accelerated beams hold significant potential is proton beam therapy. Realizing this potential, however, requires dedicated transport and focusing systems capable of shaping the beam and delivering it with well-controlled parameters. In this work, we numerically analyze the performance of a two-solenoid transport system designed to collect and focus a laser-plasma accelerated proton beam with an energy range of 8–20 MeV into a 4-mm-long cylindrical water target. The study evaluates how different solenoid current settings affect particle transport efficiency and the resulting dose distribution throughout the target depth with the goal of finding the most uniform longitudinal dose distribution.

Keywords: Laser–plasma acceleration; Proton beam transport; Solenoid focusing; Beam optics; Depth–dose distribution; Proton therapy

1. Introduction

Laser-driven ion sources offer strong potential as compact, versatile, and cost-effective alternatives to conventional accelerators, such as synchrotrons and cyclotrons. They also open the possibility for new and unique applications due to their distinctive beam properties [1, 2, 3, 4, 5, 6]. The nature of laser-target interaction allows for ion beam acceleration from emission spots with micrometer-scale effective sizes, picosecond-scale pulse durations at the source and high fluxes of 10^{11} to 10^{13} particles per shot. The broadband energy spectra of particles exhibit exponential decay, have high cut-off energies, large

[1*] National University of Science and Technology Politehnica Bucharest, Splaiul Independentei no. 313, RO-060042, Bucharest, Romania, e-mail: laura–anamaria.nita@upb.ro

[2]Technische Universität Darmstadt, Institut für Kernphysik, Schlossgartenstr. 9, 64289 Darmstadt, Germany

[3]Extreme Light Infrastructure - Nuclear Physics (ELI-NP), "Horia Hulubei" National Institute for Physics and Nuclear Engineering (IFIN-HH), 30 Reactorului Street, RO-077125 Bucharest-Măgurele, Romania

beam divergence, and acceleration gradients on the order of MeV μm^{-1} compared to MeV m^{-1} encountered in radio-frequency (RF) acceleration [7, 8, 9]. These characteristics make laser-driven ion sources highly attractive for a wide range of industrial and medical applications. In particular, their potential use in radiation therapy has drawn significant attention from the scientific community, largely because they provide straightforward access to ultra-high dose rates compatible with FLASH irradiation protocols [10, 11, 12, 13]. In addition, laser-based acceleration systems have the potential to reduce the complexity and extent of radioprotection requirements. Finally, their naturally broad ion energy spectra can facilitate the creation of a spread-out Bragg peak (SOBP), required for in-depth tumor irradiation.

Laser-driven proton sources with energies of up to 100 - 150 MeV have been reported [4, 5]. Clinical radiation treatments using proton beams require energies of up to 250 MeV, with sub-MeV precision to accurately control the in-depth dose distribution. From here now on, to successfully benefit from the tremendous advantages that come along with implementing laser-based acceleration mechanisms in clinical applications, the scientific community needs to further increase the particle energy and to develop techniques for precise spectral and angular control of the ion beam [14, 15, 16, 17].

Several dedicated laser-driven proton beamlines have been developed worldwide for radiobiological and pre-clinical radiotherapy research and are operational, such as the ELIMAIA–ELIMED platform at ELI Beamlines (Czech Republic), the CLAPA facility at Peking University (China), and the DRACO beamline at HZDR (Germany). The ELIMAIA–ELIMED beamline, driven by a petawatt laser, delivers protons in the target normal sheath acceleration regime with a maximum cutoff energy of approximately 25 MeV with potential to scale it up to 300 MeV. It employs a focusing system based on a set of five permanent-magnet quadrupoles for initial capture and rough energy selection, followed by an electromagnetic dipole chicane for narrow energy selection and two resistive quadrupoles for final beam shaping and delivery to in-air irradiation stations [18].

At Peking University, the CLAPA beamline transports protons with energies below 15 MeV via a system comprising a quadrupole triplet for collection and dipole magnets for energy selection. The planned CLAPA-II upgrade will feature higher energy protons in the range 40–100 MeV for initial radiotherapy studies, utilizing superconducting solenoids [19].

The DRACO PW laser-driven beamline at HZDR accelerates protons to cutoff energies above 70 MeV and employs a compact pulsed high-field solenoid system for chromatic focusing, energy-band selection, and transport, complemented by apertures and scatterers to produce homogeneous volumetric dose distribution at ultra-high dose rates suitable for FLASH radiobiology [20].

The Laser-hybrid Accelerator for Radiobiological Applications (LhARA) is a facility design that combines a laser-driven source with a capture system based on a plasma Gabor lens provided with an accelerator stage, enabling ultra-high dose-rate studies. It is designed for proton energies of about 10–15 MeV for in-vitro studies and up to 127 MeV for in-vivo experiments [21].

These facilities illustrate the rapid progress in combining high-intensity laser sources with advanced magnetic focusing systems to control beam divergence and energy range, to move toward clinically relevant proton energies for radiotherapy.

This paper presents a 3D simulation study of a high-current two-solenoid transport system operated at different current settings to collect and focus a laser-plasma accelerated (LPA) proton beam with energies between 8 and 20 MeV into a 4-mm-long cylindrical water sample, extending our work presented in *Nălbaru et al.* [23]. An in-depth comparison of the system's performance under the various operating conditions obtained by tuning the magnetic field of the coils is provided in terms of proton collection efficiency and resulting depth–dose profiles.

2. **Source and transport configuration**

The study was performed using COMSOL Multiphysics [22], a versatile numerical software capable of constructing detailed physical models and determining their behavior under varying conditions by solving the underlying mathematical equations. The 3D geometry feature was used to model all the components of the particle transport configuration, whose schematic representation is illustrated in Fig. 1. Two copper solenoids were defined, one with a conical shape positioned with its narrow opening toward the particle source, and another with cylindrical shape placed at a distance of 12 cm from the first one. Both coils had 70 turns, a 1 mm wire radius, a 2.5 mm axial pitch, and a maximum opening of 4 cm. The conical solenoid started with an initial opening of 1.5 cm and had a 0.4 mm radial pitch. A more detailed description of the two-solenoid beam transport configuration is provided in Ref. [23]. The logic behind the proposed system geometry is to capture and potentially focus the diverging proton beam along the length of the conical coil, as close to the source as possible.

The proton emission spot was defined as a 2 μm circle placed at 1 mm upstream of the first solenoid. The simulation was performed for a proton source with an energy range from 8 to 20 MeV with a half-angle divergence of up to 16.5°. The energy and angular proton distribution at the source is simultaneously illustrated in Fig. 2. The beam was initialized from an external file containing the position and velocity data of 2.88×10^5 macroparticles, each representing 100 physical protons, for a total of 2.88×10^7 individual particles. The initial proton distribution was generated in COMSOL Multiphysics

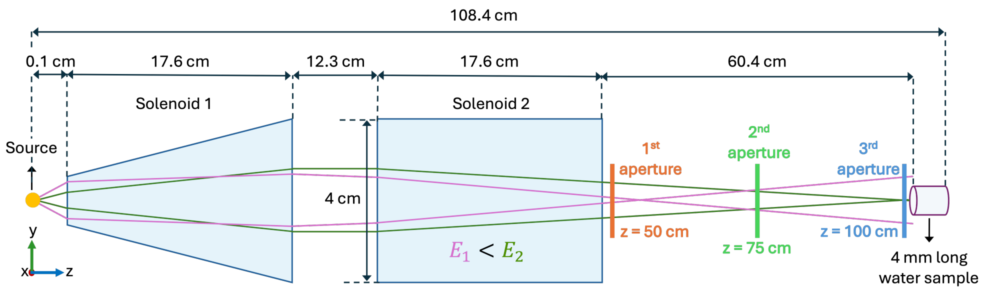

FIGURE 1. Schematic of the simulated transport configuration, consisting of a 2 μm radius proton source, a conical solenoid followed by a cylindrical solenoid (each made of 70 turns of 1 mm diameter copper wire), and a 5 mm × 4 mm (diameter × length) water sample at the end of the beamline.

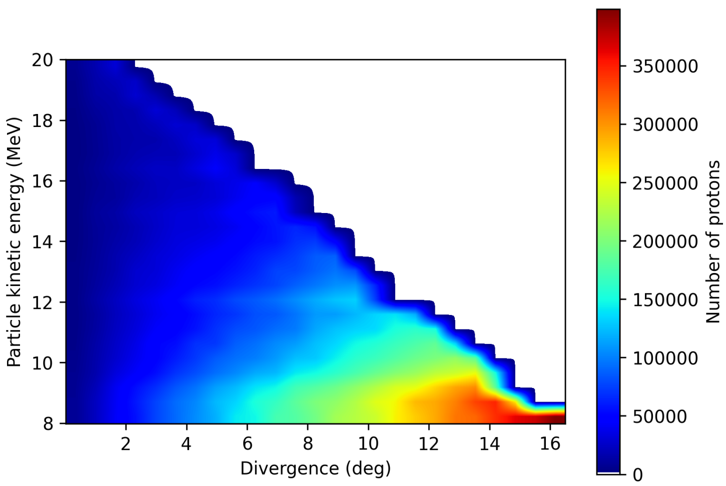

FIGURE 2. Energy and angular proton distribution at the source [24].

by performing separate simulations for discrete energies using the Inlet feature within the Charged Particle Tracing Interface, and constructing the final dataset by concatenating the extracted initial conditions (t = 0) from each run to reproduce the desired energy spectrum. Throughout this paper, all reported results refer to the total number of individual protons. The sample target was positioned approximately 1 m from the source and was modeled as a water column measuring 4 mm in length and 5 mm in diameter.

The computational workflow comprised two studies, both carried out within the *AC/DC Module* [25]. The first was a stationary analysis using the *Magnetic Fields Interface* to generate a full 3D map of the magnetic field, based on the operating currents applied to the solenoids. These results were

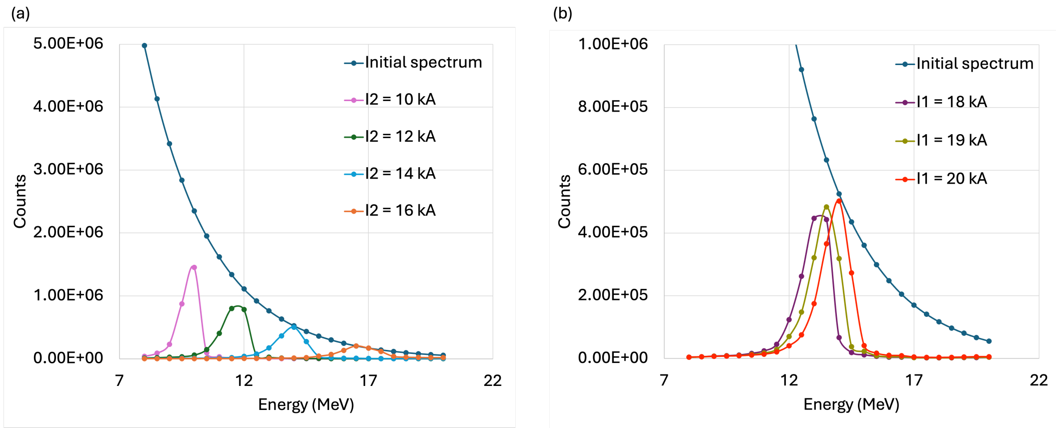

FIGURE 3. Proton energy spectrum (dark blue) shown in pan-els (a) and (b), together with the transmitted spectra across the entire target, obtained for different solenoid current configura-tions: (a) a fixed current of 20 kA applied to the first solenoid while the current of the second solenoid is set to 10, 12, 14, and 16 kA; and (b) a fixed current of 16 kA applied to the second solenoid with currents of 18, 19, and 20 kA applied to the first solenoid.

subsequently imported into a time-dependent study employing the *Charged Particle Tracing Interface* to follow the motion of individual particles as they propagated through the predetermined magnetic field.

3. Results and discussions

3.1. Proton energy spectra at the target

Our analysis first examined the effect of the solenoid operating currents on proton collection efficiency within the predefined cylindrical target. To this end, a series of simulations were performed in which the current applied to one of the two magnetic elements was varied while the operating current of the other remained fixed. With the conical solenoid current held constant at 20 kA, the current applied to the cylindrical coil was set to 10, 12, 14, and 16 kA. Fig. 3(a) presents the initially emitted proton spectrum (dark blue), together with the spectra of protons entering the target volume for each current setting. Although protons across the entire considered energy range reach the target, the contributions at some energies are several orders of magnitude lower than the dominant ones and are therefore not clearly visible at the scale used in the figure.

As the current in the second solenoid increases, the peak of the transmitted spectrum broadens and shifts toward higher energies. This behavior arises from the energy-dependent focusing properties of the magnetic fields generated by solenoids, which exert stronger focusing effects on particles of lower energies. At reduced current settings, protons in this energy range have longer focal lengths, allowing a larger fraction of them to reach the target as they get focused, as illustrated by the pink curve in Fig. 3(a), which exhibits the highest accumulation of protons with energies below 10 MeV compared to the other cases. In contrast, increasing the solenoid current shortens the focal length for these particles, causing them to be focused closer to the transport system and to become divergent by the time they reach the target. Simultaneously, the focal length of higher-energy protons is also reduced, enabling them to be focused closer to the target rather than beyond it, as occurs at lower current settings. This effect leads to the formation of peaks towards the high-energy end of the transmitted spectrum.

Table 1. Percentage of protons at the spectral peak energy interacting with the sample for different current settings applied to the first (conical) solenoid, along with the corresponding peak magnetic field values. This corresponds to the situation shown in Fig. 3(b).

Solenoid Current (kA)	18	19	20
Peak Magnetic Field (T)	8.3	8.75	9.2
Peak Energy (MeV)	13	13.5	14
Interacting Protons (%)	58	76	96

An analysis was also performed for an interchanged tuning scheme, with the second solenoid current fixed at 16 kA and the first solenoid current varied between 18, 19, and 20 kA. Under these operating conditions, the peak magnetic field ranges between 8.3 and 9.2 T, as summarized in Table 1. An example of the corresponding magnetic field distribution for a current of 20 kA is reported in Ref. [23]. The resulting transmitted spectra are shown in Fig. 3(b). While the shift toward higher proton energies is maintained, the spectral peaks become progressively narrower and increase in amplitude as the current is raised. Notably, the peaks lie much closer together, remaining confined to a similar energy range. Table 1 reports the percentage of protons interacting with the sample for each energy peak at the different current settings applied to the first solenoid. A steady increase of approximately 18–20 percentage points is observed across the cases. This increase, in both percentage and absolute value, can be explained by the progressive reduction of the focal spot size for higher-energy protons under increased solenoid current settings.

3.2. Dose distribution within the target

The current configuration shown in Fig. 3(a) was also employed for sample irradiation to investigate the resulting modifications in depth–dose profiles across eight 0.5 mm thick layers within the sample, which are illustrated in Fig. 4. The absorbed dose within the target was calculated based on the transmitted proton spectra for each case, as obtained from the particle tracing simulations and presented in Fig. 3(a). These spectra were used as input for a Python-based model to evaluate the energy deposition in the sample. The proton stopping power was derived from SRIM data [26] and approximated using the Bragg–Kleeman rule [27], resulting in the fitted expression:

$$-\frac{dE}{dx} = 28.16\ E^{-0.78}, \tag{1}$$

where dE/dx is expressed in MeV·cm^{-1} and E in MeV. The sample was divided into eight layers, and the energy deposited in each layer was computed and subsequently converted into absorbed dose by normalizing to the mass of each layer.

In all cases shown in Fig. 4, a systematic shift of the dose deposition toward greater depths is observed, reflecting changes in the transported proton energy spectra, in agreement with the results shown in Fig. 3(a). For the lowest current setting of 10 kA, the absorbed dose is primarily concentrated within the first three layers of the sample, reaching a maximum value of 1.83×10^{-1}Gy at a depth of 1.5 mm, followed by a sharp decrease. This rapid fall-off indicates that the proton population is dominated by lower-energy particles, which deposit most of their energy near the sample entrance and do not significantly penetrate deeper layers. Increasing the current by 2 kA leads to a 30–35% reduction in dose within the first three layers, while simultaneously producing a more than 30-fold increase in the absorbed dose in the fourth layer, before decreasing again at larger depths.

With an additional increase in current to 14 kA, the dose deposition shifts deeper into the sample, with the maximum absorbed dose occurring at a depth of 2.5 mm and reaching 9.89×10^{-2}Gy. Fig. 4(d) presents the most penetrating dose profile, characterized by a progressive increase in absorbed dose up to 3 mm depth, where a maximum value of 5.75×10^{-2}Gy is observed. Although the absolute dose levels accumulated in the superficial layers of the sample are lower than those obtained under the other operating conditions considered, the broader and deeper distribution indicates a more uniform delivery of higher-energy protons across the sample thickness.

3.3. Beam transport and focusing performance

An analysis of the variation in proton beam spot size along the propagation axis was also performed for four selected proton energies: 10, 12, 14 and 16 MeV. A plot of focus spot diameter as a function of position on z-axis is illustrated in Fig. 5(a). For this study, operating currents of 20 kA and 16 kA were applied to the first and second solenoids, respectively, leading to maximum magnetic field strengths of 9 T and 6 T. For all energies, the spot

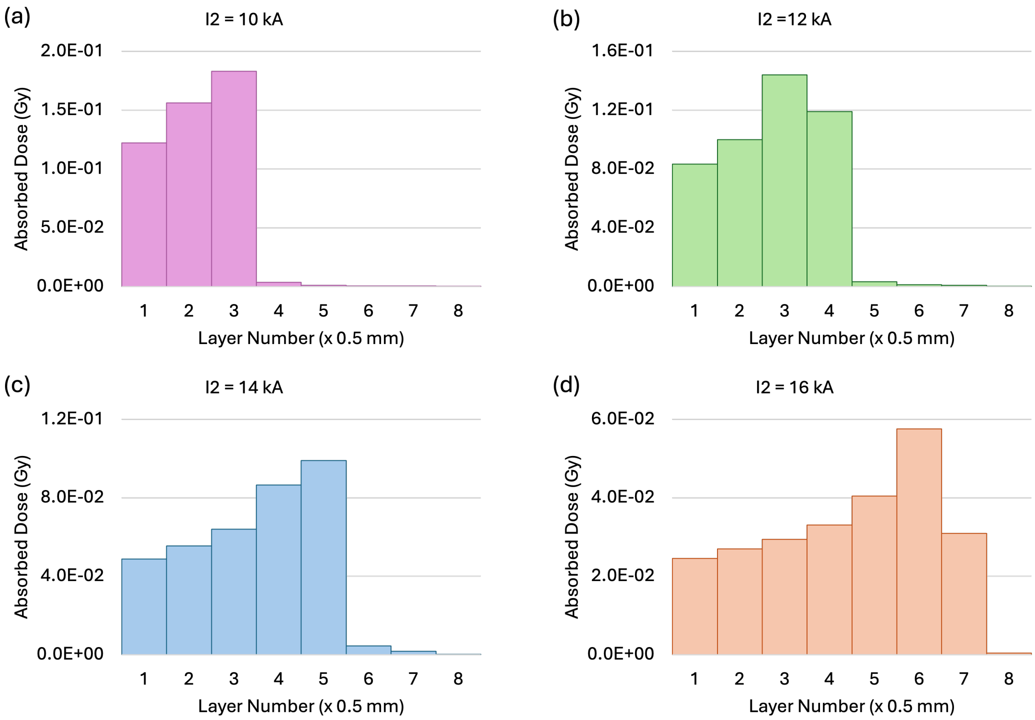

FIGURE 4. Absorbed dose distribution within the 4 mm long cylindrical water target, subdivided into eight 0.5 mm thick lay-ers, obtained after irradiation with an 8–20 MeV proton beam focused by the two-solenoid system operating at 20 kA on the first solenoid and at 10, 12, 14, and 16 kA on the second solenoid, respectively.

size exhibits a clear focusing behavior, characterized by a well-defined minimum followed by a rapid increase downstream of the focal position. Across the investigated energies, the minimum beam spot size ranges from approximately 3.6 to 4.4 mm, while the corresponding focal position shifts downstream from about 0.60 m to 0.95 m as the proton energy increases. Overall, although the minimum achievable spot sizes remain of comparable magnitude for all examined energies, the systematic shift of the focal position along the propagation axis highlights the strong energy dependence of the beam transport and focusing system.

The centroid trajectories in the transverse plane were analyzed by plotting the horizontal centroid position as a function of the vertical centroid position for the four proton energies considered (10, 12, 14, and 16 MeV). As shown in Fig. 5(b), all energies exhibit smooth and predominantly linear trajectories, indicating a well-defined and stable steering behavior. Lower-energy protons display larger transverse excursions, consistent with their stronger response to the solenoidal magnetic fields. A decrease in slope of the centroid

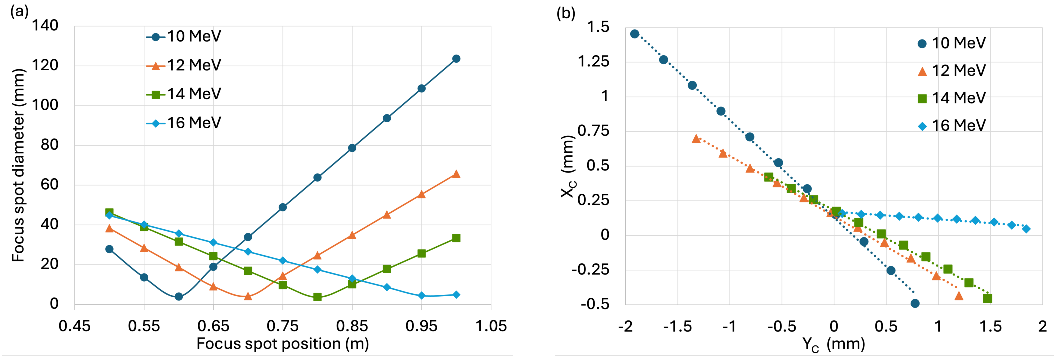

FIGURE 5. (a) Evolution of the focal spot diameter along the propagation axis for four proton energies (10, 12, 14, and 16 MeV) after focusing by the two-solenoid system operating at currents of 20 kA and 16 kA, respectively. (b) Corresponding centroid trajectories in the transverse plane for the same proton energies and focusing conditions.

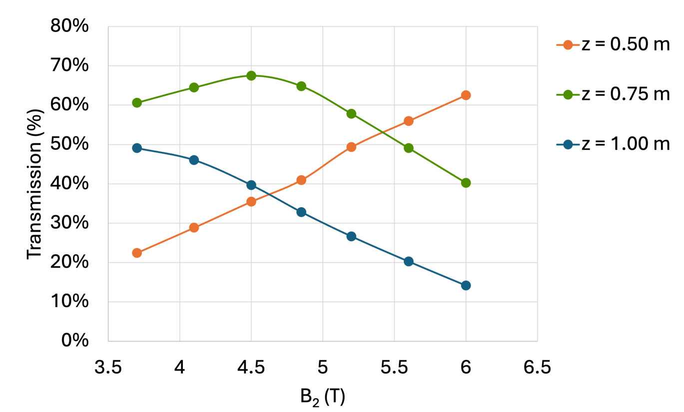

FIGURE 6. Transmission through a 20 mm diameter aperture for three focal distances as a function of the magnetic field B2 generated by the second solenoid.

trajectory is observed with increasing proton energy. While slopes in the range -0.7 to -0.4 are observed for protons from 10 to 14 MeV, the highest-energy case exhibits a substantially reduced slope of approximately -0.055, reflecting a significantly weaker transverse steering response associated with increased magnetic rigidity. The observed shift of the spot centroid in the y-direction at higher energies is an artifact arising from the statistical distribution of particles in the beam with respect to energy and divergence angle. The absence of curvature or spiral features in the centroid trajectories indicates that the observed steering is dominated by a simple beam tilt rather than by transverse coupling or rotational motion.

A further investigation was conducted to assess the influence of the magnetic field on particle transmission rates through a 20 mm diameter aperture positioned at three different locations along the propagation axis relative to the source. An aperture diameter of 20 mm was selected as a compromise between maximizing proton beam transmission and optimizing spectral selection. For this study, the current on the conical solenoid was held constant to 20 kA, while the current applied to the cylindrical solenoid was varied between 10 and 16 kA, with a 1 kA step, resulting in a magnetic field with values ranging from 3.7 to 6 T. The aperture positions along the z-axis were 0.5, 0.75, and 1 m, as shown in Fig. 1. Fig. 6 shows the particle transmission through the aperture, evaluated immediately downstream of it, as a function of the magnetic field generated by the second solenoid at the previously mentioned positions, considering the full 8–20 MeV spectrum. At the closest position to the solenoid system, z = 0.5 m, illustrated with orange in Fig. 6, a quasi-linear increase of the transmission rates with the increase of the magnetic field can be observed. Higher values of the magnetic filed induce stronger focusing and reduce the focal lengths, resulting in a steady increase in the number of particles that pass trough the aperture.

When the aperture is placed 25 cm further away from the system (plot represented with green), the transmission rates firstly increase, meeting their maximum value of a little under 70 % for a magnetic filed of 4.5 T, to then decrease to around 40 %. This behavior is caused by the lower energetic particles, which under the influence of stronger magnetic fields focus before reaching the aperture, leading to divergent profiles at the aperture position and causing particle loss. An additional displacement of the aperture by another 25 cm in the propagation direction, results in transmission rates of under 50 %, characterized by a decreasing profile with a minimum of 14 %, driven by the increase in the divergence of the lower energetic particles, which are also the most abundant.

4. **Conclusions**

This work presents a simulation-based performance analysis of a high-current two-solenoid transport system designed to collect and focus LPA proton beams with energies up to 20 MeV. Various combinations of operating currents between 10 and 20 kA were applied to the two solenoids and systematically analyzed. The results demonstrate that variations in the current of the second solenoid play a key role in shaping and selecting the transmitted proton energy spectrum, enabling peak formation toward the high-energy region, while variations in the current of the first conical solenoid lead to the formation of narrower spectral peaks within a similar energy range.

The depth–dose distributions, evaluated in 0.5-mm-thick layers within a cylindrical water target, reveal non-uniform dose deposition, with absorbed dose values reaching several hundreds of mGy. In all cases, the dose deposition profile exhibits a systematic shift toward greater depths with increasing current in the second solenoid, consistent with the transmission of higher-energy proton spectra. The maximum absorbed dose in one 0.5 mm thick layer obtained across all cases is 9.89×10^{-2}Gy, occurring at a depth of 2.5 mm for current values of 20 kA and 14 kA applied to the first and second solenoids, respectively.

The focal spot size measured along the propagation axis remains on the millimeter scale for the investigated energies, with minimum values between 3.6 and 4.4 mm, reflecting the strong influence of proton energy on the beam transport and focusing system. An analysis of the particle transmission rates through a 20 mm diameter aperture, placed at three focal distances as a function of the magnetic field of the second solenoid, showed a maximum transmission of 70% for a magnetic field of 4.5 T at a distance of 0.75 m from the proton emission spot. Further downstream displacement of the aperture leads to a significant reduction in transmission, dropping below 50% due to increased beam divergence, particularly of the lower-energy protons.

5. **Acknowledgments**

This work is supported by the Deutsche Forschungs- gemeinschaft (DFG, German Research Foundation)— Project-ID 499256822—GRK 2891 “Nuclear Photonics” and by Projects `ELI-RO/DFG/2025_013` IATP-NP 2.0 and ELI-RO_19 `HighProtonPLas` funded by the Institute of Atomic Physics, Romania and The Government of Romania, through the Health Program, under the project “Medical Applications of High-Power Lasers – Dr. LASER”.

REFERENCES

[1] *S.C. Wilks, A.B. Langdon, T.E. Cowan, M. Roth, M. Singh, S. Hatchett, M.H. Key, D. Pennington, A. MacKinnon, and R.A. Snavely*, Energetic proton generation in ultra-intense laser–solid interactions , Phys. Plasmas, **8** (2001), 542.

[2] *B.M. Hegelich, B.J. Albright, J. Cobble, et al.*, Laser acceleration of quasi-monoenergetic MeV ion beams, Nature. **439** (2006), 441–444.

[3] *J. Fuchs, P. Antici,E. d'Humières, E. Lefebvre, M. Borghesi, E. Brambrink, C.A. Cecchetti, et al.*, Laser-driven proton scaling laws and new paths towards energy increase. Nature Phys., **2**(2006), 48.

[4] *Y. Shou, X. Wu, K.H. Pae, G.-E. Ahn, S.Y. Kim, S.H. Kim, J.W. Yoon et al.*, Laser-driven proton acceleration beyond 100 MeV by radiation pressure and Coulomb repulsion in a conduction-restricted plasma. Nat. Commun., **16** (2025), 1487.

[5] *T. Ziegler, I. Gothel, S. Assenbaum et al.*, Laser-driven high-energy proton beams from cascaded acceleration regimes, Nat. Phys. , **20**(2024), No. 1211.

[6] *K.A. Tanaka, K. M. Spohr, D.L. Balabanski, S. Balascuta, L. Capponi, M.O. Cernainau, M. Cuciuc, A. Cucoanes, I. Dancus, A. Dhal, et al.*, Matter and Rad. Extremes, **5** (2020), 024402.

[7] *H. Daido1, M. Nishiuchi, A.S. Pirozhkov*, Review of laser-driven ion sources and their applications, Rep. Prog. Phys., **75** (2012), 056401.

[8] *A. Macchi, M. Borghesi, M. Passoni*, Ion acceleration by superintense laser-plasma interaction, Rev. Mod. Phys., **85** (2013), No. 2, 751-793.

[9] *M. Roth, M. Schollmeier*, Ion Acceleration—Target normal Sheath Acceleration. In: B Holzer, editor. Proceedings of the CAS-CERN Accelerator School: Plasma Wake Acceleration; 23–29 November 2014; Geneva, Switzerland. SPIE (2016).

[10] *M.-C. Vozenin, J. Bourhis and M. Durante*, Towards clinical translation of FLASH radiotherapy, Nat Rev Clin Oncol, **19**(2022), No. 791.

[11] *K. Zeil, M. Baumann, E. Beyreutheret, et al.*, Dose-controlled irradiation of cancer cells with laser-accelerated proton pulses, Applied Physics B, **110**(2013), No. 437.

[12] *J. Bin, L. Obst-Huebl, L., J.H. Mao et al.*, A new platform for ultra-high dose rate radiobiological research using the BELLA PW laser proton beamline. Sci Rep, **12** (2022), 1484.

[13] *S. Rudigkeit, T.E. Schmid, A.C. Dombrowsky et al.* Proton-FLASH: effects of ultra-high dose rate irradiation on an in-vivo mouse ear model. Sci. Rep., **14** (2024), 1418.

[14] *K. Zeil, S.D. Kraft, S. Bock, M. Bussmann, T.E. Cowan, T. Kluge, et al.*, The Scaling of Proton Energies in Ultrashort Pulse Laser Plasma Acceleration, New J. Phys., **12** (2010), 045015.

[15] *S. Keppler, N. Elkina, G. A. Becker, J. Hein, M. Hornung , Mausezahl, C. Rodel, I. Tamer, M. Zepf, M.C. Kaluza*, Intensity scaling limitations of laser-driven proton acceleration in the TNSA-regime, Phys. Rev. Res **4** (2022), 013065.

[16] *A. Magureanu, L. Dinca, C. Jalba, R.F. Andrei, I. Burducea, D.G. Ghita, V. Nastasa, et al.*, Target Characteristics Used in Laser-Plasma Acceleration of Protons Based on the TNSA Mechanism, Front. Phys., **10** (2022), 727718.

[17] *M.O. Cernaianu et al.*,Commissioning of the 1 PW experimental area at ELI-NP using a short focal parabolic mirror for proton acceleration,Matter Radiat. Extremes, **10** (2025), No. 2.

[18] *D. Margarone et al.*, ELIMAIA: A Laser-Driven Ion Accelerator for Multidisciplinary Applications, Quantum Beam Sci. **2** (2018), 8.

[19] *K.D. Wang et al.*, Beam distribution homogenization design for laser-driven proton therapy accelerator, Nucl. Instrum. Methods Phys. Res. A **1040** (2022) 167196.

[20] *J. Metzkes-Ng et al.*, The Dresden platform is a research hub for ultra-high dose rate radiobiology. Sci Rep **13** (2023), 20611 .

[21] *G. Aymar et al.*, LhARA: The Laser-hybrid Accelerator for Radiobiological Applications. Front. Phys. **8** (2020), 567738.

[22] COMSOL Inc., Multiphysics® v. 6.1. www.comsol.com. COMSOL AB, Stockholm, Sweden, www.comsol.com

[23] *L. Nălbaru, and M. Arnold, and C. Ticoş*, Conical coil focusing of laser-plasma accelerated proton beams for applications, Phys. Rev. Accel. Beams, **28**(2025), No. 114701.

[24] *F. Nuernberg, M. Schollmeier, E. Brambrink, et al.*, Radiochromic film imaging spectroscopy of laser-accelerated proton beams, Rev. Sci. Instrum., **80** (2009), 033301.

[25] AC/DC Module User's Guide, COMSOL Multiphysics® v. 6.1, COMSOL AB, Stockholm, Sweden, 2022.

[26] *J. Ziegler, M. Ziegler, and J. Biersak*, SRIM – the stopping and range of ions in matter, Nucl. Instr. Meth. Phys. Res., Sect. B 268, 1818 (2010)

[27] *W. Ulmer*, Theoretical aspects of energy–range relations, stopping power and energy straggling of protons, Radiation Physics and Chemistry 76, 1089 (2007)